

# Accurate calculation of the local density of optical states in inverse-opal photonic crystals

Ivan S. Nikolaev,<sup>1</sup> Willem L. Vos,<sup>1,2</sup> and A. Femius Koenderink<sup>1,\*</sup>

<sup>1</sup>Center for Nanophotonics, FOM Institute for Atomic and Molecular Physics (AMOLF), Kruislaan 407, NL-1098SJ Amsterdam, The Netherlands

<sup>2</sup>Complex Photonic Systems (COPS), MESA<sup>+</sup> Institute for Nanotechnology, NL-7500 AE Enschede, University of Twente, The Netherlands

\*Corresponding author: f.koenderink@amolf.nl

Received January 8, 2009; revised March 2, 2009; accepted March 6, 2009;  
posted March 10, 2009 (Doc. ID 105720); published April 10, 2009

We have investigated the local density of optical states (LDOS) in titania and silicon inverse opals—three-dimensional photonic crystals that have been realized experimentally. We used the H-field plane-wave expansion method to calculate the density of states and the projected LDOS, which are directly relevant for spontaneous emission dynamics and strong coupling. We present the first quantitative analysis of the frequency resolution and of the accuracy of the calculated LDOS. We have calculated the projected LDOS for many different emitter positions and orientations in inverse opals in order to supply a theoretical interpretation for recent emission experiments and as reference results for future experiments and theory by other workers. The results show that the LDOS in inverse opals strongly depends on the crystal lattice parameter as well as on the position and orientation of emitting dipoles. © 2009 Optical Society of America

OCIS codes: 160.5298, 260.2510, 270.5580, 290.4210.

## 1. INTRODUCTION

Photonic crystals are metamaterials with periodic variations of the dielectric function on length scales comparable to the wavelength of light. These dielectric composites are of keen interest for scientists and engineers because they offer exciting ways to manipulate photons [1,2]. Of particular interest are three-dimensional (3D) photonic crystals possessing a photonic bandgap, i.e., a frequency range where no photon modes exist at all. Photonic bandgap materials possess great potential for drastically changing the rate of spontaneous emission and for achieving localization of light [3–6]. Control over spontaneous emission is important for many applications such as miniature lasers [7], light-emitting diodes [8], and solar cells [9]. According to Fermi's Golden Rule, the rate of spontaneous emission from quantum emitters such as atoms, molecules, or quantum dots is proportional to the "local radiative density of states" (LDOS) [10,11], which counts the number of electromagnetic states at a given frequency, location and orientation of the dipolar emitters. In addition, nonclassical effects can occur that are beyond Fermi's Golden Rule [2,11], such as fractional decay. These strong coupling phenomena rely on coherent coupling of the quantum emitter to a sharp feature in a highly structured LDOS. Whether these effects are in fact observable in real photonic crystals depends on how rapidly the LDOS changes within a small frequency window [12]. Therefore LDOS calculations for experimentally realized photonic crystals are essential to assess current spontaneous emission experiments and future strong cou-

pling experiments alike, provided that the calculations are accurate and have a controlled frequency resolution.

LDOS effects on spontaneous emission in photonic crystals have been experimentally demonstrated in a variety of systems. Since only 3D crystals promise full control over all optical modes with which elementary emitters interact, many groups have pursued 3D photonic crystals. Fabrication of such periodic structures with high photonic strengths is, however, a great challenge [2,13]. Inverse opals, which can be fabricated relatively easily using self-assembly methods, are among the few 3D photonic crystals that sustain complete photonic bandgaps. Such crystals consist of *fcc* lattices of close-packed air spheres in a backbone material with a high refractive index [14–18]. In these inverse opals, CW experiments on light sources with a low quantum efficiency revealed evidence of inhibited radiative emission rates [19,20]. In time-resolved fluorescence experiments using emitters with high quantum efficiencies, both enhanced and inhibited fluorescence decay rates have been observed [21]. In parallel to these experiments on 3D crystals, several groups have realized that emission enhancement and partial inhibition can also be obtained in 2D slab structures [22–26].

Following the first calculations by Suzuki and Yu [27], several papers have reported calculations of the LDOS in photonic crystals using both time domain [28–30] and frequency domain methods [31–34]. It is not straightforward to use such calculations for interpreting experiments. Even if one assumes that infinite-system calculations for

perfect crystals are a valid starting point for interpreting experiments, one quickly realizes that available calculations are not satisfactory due to several problems in the literature:

1. Most prior calculations were performed for model systems that do not correspond at all to structures used in experiments, and for emitter positions that are not probed in experiments.

2. The accuracy of the reported LDOS has never been discussed, hampering comparison with experiments.

3. The frequency resolution of the reported LDOS has remained unspecified. Therefore sharp features of relevance for nonclassical emission can not be assessed [11,12].

4. Many previously reported LDOS calculations are erroneous for symmetry reasons, as pointed out by Wang *et al.* [33]. These errors are quantitatively and qualitatively large, with different functional dependencies on frequency, and up to tenfold differences in LDOS.

In this paper we aim to overcome all these problems. We benchmark the accuracy and frequency resolution for our LDOS calculations. Since prior LDOS calculations are scarce and partly erroneous (item 4 above) we present sets of LDOS results for experimentally relevant structures and for spatial positions where sources can be practically placed. Specifically, we model the spatial distribution of the dielectric function  $\epsilon(\mathbf{r})$  in such a way that it closely resembles  $\epsilon(\mathbf{r})$  in titania (TiO<sub>2</sub>) [14,15] and silicon (Si) inverse-opal photonic crystals [17,18]. For these two structures we calculate the LDOS at various positions in the crystal unit cell and for specific orientations of the transition dipoles. The results on the TiO<sub>2</sub> inverse opals are relevant for interpreting recent emission experiments [21,35]. To aid other workers to interpret their experiments and to benchmark their codes, we make the data sets that we report available as online material.

For interpretation of experiments, we note that the calculations presented here are correct for infinite, perfect, lossless crystals, whereas crystals in real experiments suffer from finite size, optical absorption, and copious extinction by disorder-induced scattering [36]. Given the efforts undertaken to ensure that only sources deep inside crystals are probed [19], the main deviations from real crystals to modeled crystals can be captured by the extinction length, typically  $\geq 100$  times the lattice constant [36]. Such extinction can be treated perturbatively [37] and causes weak broadening of LDOS features by approximately  $10^{-2}$  relative bandwidth and deviations of a few percent in the LDOS associated with propagating bands. While dissipation formally closes bandgaps, bandgaps are expected to be exponentially robust against extinction lengths exceeding 5 to 10 lattice constants [30,37]. Barring pathological resonances due to scattering or Fabry–Pérot type size resonances in extremely small perfect crystals [30], we therefore expect that infinite system calculations are relevant for experimental data.

The paper is arranged as follows. In Section 2, we present a detailed description of the method by which we have calculated the photonic band structures and the LDOS. We discuss the accuracy and frequency resolution of our calculations. In Section 3 we compare our compu-

tations with the known DOS in vacuum and with earlier results on the DOS and LDOS [33] in 3D periodic structures. Section 4 describes the LDOS in inverse opals from TiO<sub>2</sub>, and in Section 5 we present results of the LDOS in Si inverse-opal photonic bandgap crystals.

## 2. CALCULATION OF LOCAL DENSITY OF STATES

### A. Introduction

The LDOS is defined as

$$N(\mathbf{r}, \omega, \mathbf{e}_d) = \frac{1}{(2\pi)^3} \sum_n \int_{BZ} d\mathbf{k} \delta(\omega - \omega_{n,\mathbf{k}}) |\mathbf{e}_d \cdot \mathbf{E}_{n,\mathbf{k}}(\mathbf{r})|^2, \quad (1)$$

where integration over the  $\mathbf{k}$  vector is performed over the first Brillouin zone,  $n$  is the band index, and  $\mathbf{e}_d$  is the orientation of the emitting dipole. The total DOS is the unit-cell and dipole-orientation average of the LDOS defined as  $N(\omega) = \sum_n \int_{BZ} d\mathbf{k} \delta(\omega - \omega_{n,\mathbf{k}})$ . The important quantities that determine the LDOS are the eigenfrequencies  $\omega_{n,\mathbf{k}}$  and electric field eigenmodes  $\mathbf{E}_{n,\mathbf{k}}(\mathbf{r})$  for each  $\mathbf{k}$  vector. Calculation of these parameters will be discussed below in Subsection 2.B.

The expression for the LDOS contains the term  $|\mathbf{e}_d \cdot \mathbf{E}_{n,\mathbf{k}}(\mathbf{r})|^2$  that depends on the dipole orientation  $\mathbf{e}_d$ . It is important to realize that in photonic crystals the vector fields  $\mathbf{E}_{n,\mathbf{k}}(\mathbf{r})$  are not invariant under the lattice point-group operations  $\alpha$ , as first reported in [33]. Explicitly, this means that the projection of the field of a mode at wave vector  $\mathbf{k}$  on the dipole orientation  $\mathbf{e}_d$ , [i.e.,  $|\mathbf{e}_d \cdot \mathbf{E}_{n,\mathbf{k}}(\mathbf{r})|$ ], is not identical to  $|\mathbf{e}_d \cdot \mathbf{E}_{n,\alpha[\mathbf{k}]}(\mathbf{r})|$ , i.e., the projection of the symmetry related modes with wave vectors  $\alpha[\mathbf{k}]$  on the same  $\mathbf{e}_d$ . As a consequence one cannot calculate the LDOS for a specific dipole orientation by restricting the integral over the Brillouin zone in Eq. (1) to just the irreducible part (1/48th) of the Brillouin zone, since symmetry-related wave vectors do not give identical contributions. Unfortunately, in many previous reports on the LDOS, this reduced symmetry for vector modes as compared with scalar quantities was overlooked, resulting in erroneous results [33]. In general, the only symmetry that can be invoked to avoid using the full Brillouin zone for LDOS calculations is inversion symmetry, which corresponds to time-reversal symmetry. Consequently, correct results require that exactly half of the Brillouin zone be considered for LDOS calculations, rather than the irreducible part of the Brillouin zone that was used in most previous literature. We have explicitly verified that our implementation (using the  $k_z \geq 0$  half of the Brillouin zone) results in the same LDOS on symmetry-related positions, provided that one also takes the concomitant symmetry related dipole orientation into account. Furthermore, our calculations confirm the claim by Wang *et al.* [33] that this required symmetry is recovered only upon integration over half the Brillouin zone, rather than over just the irreducible part as considered in, e.g., [31,32].

### B. Plane-Wave Expansion

We use the H-field inverted plane-wave expansion method [31,38,39] to solve for the electromagnetic field modes in

photonic crystals. For nonmagnetic materials, it is most convenient to solve the wave equation for the  $\mathbf{H}(\mathbf{r})$  field [40]

$$\nabla \times [\epsilon(\mathbf{r})^{-1} \nabla \times \mathbf{H}(\mathbf{r})] = \frac{\omega^2}{c^2} \mathbf{H}(\mathbf{r}), \quad (2)$$

because the operator  $\nabla \times \epsilon(\mathbf{r})^{-1} \nabla \times$  is Hermitian. Consequently, Eq. (2) can be interpreted as an eigenvalue problem with real eigenvalues  $\omega^2/c^2$  [1,31,38,39], with the proviso that  $\epsilon(\mathbf{r})$  is real and frequency independent. While lossless Drude models for dispersion in the dielectric function can also be included [41], more general dispersion relations for  $\epsilon$  do not allow Eq. (2) to be written as an eigenvalue problem. Because of the periodicity of the dielectric function  $\epsilon(\mathbf{r})$  in photonic crystals, the field modes  $\mathbf{H}_{\mathbf{k}}(\mathbf{r})$  of the eigenvalue problem Eq. (2) satisfy the Bloch theorem [42]:

$$\mathbf{H}_{\mathbf{k}}(\mathbf{r}) = e^{i\mathbf{k}\cdot\mathbf{r}} \mathbf{u}_{\mathbf{k}}(\mathbf{r}). \quad (3)$$

These Bloch modes are fully described by the wave vector  $\mathbf{k}$  and the periodic function  $\mathbf{u}_{\mathbf{k}}(\mathbf{r})$ , which has the periodicity of the crystal lattice so that  $\mathbf{u}_{\mathbf{k}}(\mathbf{r}) = \mathbf{u}_{\mathbf{k}}(\mathbf{r} + \mathbf{R})$ . To solve the wave equation, the inverse dielectric function and the Bloch modes are expanded in a Fourier series over the reciprocal-lattice vectors  $\mathbf{G}$ :

$$\epsilon(\mathbf{r})^{-1} = \eta(\mathbf{r}) = \sum_{\mathbf{G}} \eta_{\mathbf{G}} e^{i\mathbf{G}\cdot\mathbf{r}}, \quad (4)$$

$$\mathbf{H}_{\mathbf{k}}(\mathbf{r}) = \sum_{\mathbf{G}} \mathbf{u}_{\mathbf{G}}^{\mathbf{k}} e^{i(\mathbf{k}+\mathbf{G})\cdot\mathbf{r}}, \quad (5)$$

where  $\eta_{\mathbf{G}}$  and  $\mathbf{u}_{\mathbf{G}}^{\mathbf{k}}$  are the 3D Fourier expansion coefficients of, respectively,  $\eta(\mathbf{r})$  and  $\mathbf{u}_{\mathbf{k}}(\mathbf{r})$ .

Substituting these expressions into the H-field wave equation in Eq. (2), we obtain the linear set of eigenvalue equations

$$\begin{aligned} & - \sum_{\mathbf{G}'} \eta_{\mathbf{G}-\mathbf{G}'} (\mathbf{k} + \mathbf{G}) \times [(\mathbf{k} + \mathbf{G}') \times \mathbf{u}_{\mathbf{G}'}^{\mathbf{k}}] \\ & = \frac{\omega_n^2(\mathbf{k})}{c^2} \mathbf{u}_{\mathbf{G}}^{\mathbf{k}}. \end{aligned} \quad (6)$$

This infinite equation set with the known parameters  $\mathbf{G}$  and  $\eta_{\mathbf{G}-\mathbf{G}'}$  determines all allowed frequencies  $\omega_n(\mathbf{k})$  for each value of the wave vector  $\mathbf{k}$ , subject to the transversality requirement  $\nabla \cdot \mathbf{H}_{\mathbf{k}}(\mathbf{r}) = 0$ . Because of the periodicity of  $\mathbf{u}_{\mathbf{k}}(\mathbf{r})$ , we can restrict  $\mathbf{k}$  to the first Brillouin zone. For each wave vector  $\mathbf{k}$ , there is a countably infinite number of modes with discretely spaced frequencies. All the modes are labeled with the band number  $n$  in order of increasing frequency and are described as a family of continuous functions  $\omega_n(\mathbf{k})$  of  $\mathbf{k}$ .

To compute the eigenfrequencies  $\omega_n(\mathbf{k})$  and the expansion coefficients of the eigenmodes  $\mathbf{u}_{\mathbf{G}}^{\mathbf{k}}$ , the infinite equation set is truncated. By restricting the number of reciprocal-lattice vectors  $\mathbf{G}$  to a finite set  $\mathcal{G}$  with  $N_{\mathcal{G}}$  elements, Eq. (6) is limited to a  $3N_{\mathcal{G}}$ -dimensional equation set. In our implementation we choose the truncated set  $\mathcal{G}$  to correspond to the set of all reciprocal lattice vectors within a sphere centered around the origin of  $\mathbf{k}$  space. The

transversality of the H field gives an additional condition on the eigenmodes:  $(\mathbf{k} + \mathbf{G}) \cdot \mathbf{u}_{\mathbf{G}}^{\mathbf{k}} = 0$ , which eliminates one vector component of  $\mathbf{u}_{\mathbf{G}}^{\mathbf{k}}$ . Following [31], for each  $\mathbf{k} + \mathbf{G}$  one needs to find two orthogonal unit vectors  $\mathbf{e}_{\mathbf{k}+\mathbf{G}}^{1,2}$  that form an orthogonal triad with  $\mathbf{k} + \mathbf{G}$ . By expressing the eigenmode expansion coefficients in the plane normal to  $\mathbf{k} + \mathbf{G}$  as  $\mathbf{u}_{\mathbf{G}}^{\mathbf{k}} = u_{\mathbf{G},1}^{\mathbf{k}} \mathbf{e}_{\mathbf{k}+\mathbf{G}}^1 + u_{\mathbf{G},2}^{\mathbf{k}} \mathbf{e}_{\mathbf{k}+\mathbf{G}}^2$ , we remove one-third of the unknowns. Then, Eq. (6) becomes

$$\begin{aligned} & \sum_{\mathbf{G}' \in \mathcal{G}} \eta_{\mathbf{G}-\mathbf{G}'} |\mathbf{k} + \mathbf{G}| |\mathbf{k} + \mathbf{G}'| \\ & \cdot \left\{ \begin{bmatrix} \mathbf{e}_{\mathbf{k}+\mathbf{G}}^2 \cdot \mathbf{e}_{\mathbf{k}+\mathbf{G}'}^2 & -\mathbf{e}_{\mathbf{k}+\mathbf{G}}^2 \cdot \mathbf{e}_{\mathbf{k}+\mathbf{G}'}^1 \\ -\mathbf{e}_{\mathbf{k}+\mathbf{G}}^1 \cdot \mathbf{e}_{\mathbf{k}+\mathbf{G}'}^2 & \mathbf{e}_{\mathbf{k}+\mathbf{G}}^1 \cdot \mathbf{e}_{\mathbf{k}+\mathbf{G}'}^1 \end{bmatrix} \begin{pmatrix} u_{\mathbf{G}',1}^{\mathbf{k}} \\ u_{\mathbf{G}',2}^{\mathbf{k}} \end{pmatrix} \right\} \\ & = \frac{\omega_n^2(\mathbf{k})}{c^2} \begin{pmatrix} u_{\mathbf{G},1}^{\mathbf{k}} \\ u_{\mathbf{G},2}^{\mathbf{k}} \end{pmatrix}, \quad \forall \mathbf{G} \in \mathcal{G}. \end{aligned} \quad (7)$$

To find the matrix of Fourier coefficients  $\eta_{\mathbf{G}-\mathbf{G}'}$ , we use the method of [31,38]. The coefficients are computed by first Fourier-transforming the dielectric function  $\epsilon(\mathbf{r})$  and then truncating and inverting the resulting matrix. As first noted by Ho *et al.* [38], using the inverse of  $\epsilon_{\mathbf{G}-\mathbf{G}'}$  rather than  $\eta_{\mathbf{G}-\mathbf{G}'}$  dramatically improves the (poor) convergence of the plane-wave method that is associated with the discontinuous nature of the dielectric function [39]. A rigorous explanation for this improvement was put forward by Li [43], who studied the presence of Gibbs oscillations in the truncated Fourier expansion of products of functions with complementary jump discontinuities. Using the H-field inverted-matrix plane-wave method, the frequencies obtained with  $N_{\mathcal{G}} = 725$  (for *fcc* structures) deviate by less than 0.5% from the converged band structures for the lowest ten bands [31].

Solving Eqs. (7) gives the frequencies  $\omega_n(\mathbf{k})$  and the Fourier expansion coefficients for the H-field eigenmodes  $\mathbf{H}_{n,\mathbf{k}}(\mathbf{r})$  needed to calculate the LDOS in the photonic crystal. The required E fields  $\mathbf{E}_{n,\mathbf{k}}(\mathbf{r})$  are obtained using the Maxwell equation  $\partial \mathbf{D} / \partial t = \nabla \times \mathbf{H}$ :

$$\begin{aligned} \mathbf{E}_{n,\mathbf{k}}(\mathbf{r}) & = \frac{1}{\omega_n(\mathbf{k}) \epsilon_0} \sum_{\mathbf{G}, \mathbf{G}' \in \mathcal{G}} \eta_{\mathbf{G}'-\mathbf{G}} |\mathbf{k} + \mathbf{G}| \\ & \cdot [(u_{\mathbf{G},1}^{\mathbf{k}} \mathbf{e}_{\mathbf{k}+\mathbf{G}}^2 - u_{\mathbf{G},2}^{\mathbf{k}} \mathbf{e}_{\mathbf{k}+\mathbf{G}}^1) e^{i(\mathbf{k}+\mathbf{G}')\cdot\mathbf{r}}]. \end{aligned} \quad (8)$$

From the orthonormality of the eigenvectors of Eqs. (7) it follows that the Bloch functions  $\mathbf{H}_{n,\mathbf{k}}(\mathbf{r})$  and  $\mathbf{E}_{n,\mathbf{k}}(\mathbf{r})$  defined above satisfy the orthonormality relations

$$\int_{\text{BZ}} \mathbf{H}_{n,\mathbf{k}}(\mathbf{r}) \cdot \mathbf{H}_{n',\mathbf{k}'}^*(\mathbf{r}) d\mathbf{r} = \delta(\mathbf{k} - \mathbf{k}') \delta_{n,n'}, \quad (9)$$

$$\int_{\text{BZ}} \epsilon(\mathbf{r}) \mathbf{E}_{n,\mathbf{k}}(\mathbf{r}) \cdot \mathbf{E}_{n',\mathbf{k}'}^*(\mathbf{r}) d\mathbf{r} = \delta(\mathbf{k} - \mathbf{k}') \delta_{n,n'}. \quad (10)$$

It should be noted in the definition of  $\mathbf{E}_{n,\mathbf{k}}$  that the multiplication by  $1/\epsilon(\mathbf{r})$  to calculate  $\mathbf{E}$  from  $\mathbf{D}$  is not in the denominator in front of the Fourier expansion. Rather it appears as a matrix multiplying the  $\mathbf{D}$  field in Fourier space, i.e., within the sum over reciprocal lattice vectors. This ordering ensures that complementary jumps in  $\mathbf{D}$  and  $1/\epsilon(\mathbf{r})$  cancel even for the truncated Fourier series

[43], as can be easily checked by plotting calculated mode profiles for TM modes in 2D crystals.

### C. Frequency Resolution and Accuracy of LDOS

We are not aware of any previous report that benchmarks the accuracy of the calculated LDOS or that specifies the frequency resolution. Motivated by the requirements for accurate results for comparison with experiments and for judging the utility of crystals for nonclassical emission dynamics, we consider the accuracy and resolution of approximations to the LDOS integral in Eq. (1). The main approximation is to replace the integration over wave vector  $\mathbf{k}$  by an appropriately weighted summation over a discrete set of wave vectors on a discretization grid. Either interpolation schemes [31] or histogramming (“root sampling”) methods are used that are based on weighted summations over special k-point grids, as introduced by Monkhorst and Pack [44]. The k-point grid density sets the number  $N_k$  of k-points in the Brillouin zone. The accuracy of the resulting LDOS approximation is set by the density of grid points that is used to discretize the wave vector integral.

Because of the transparent relation among the accuracy of the DOS, the frequency resolution, and the  $\mathbf{k}$ -vector sampling resolution, we have focused on the simple histogramming approach using Monkhorst and Pack’s special points and weights [44]. For the LDOS computations one chooses a certain frequency bin width  $\Delta\omega$  to build an LDOS histogram. For a desired frequency resolution  $\Delta\omega$  and a desired accuracy for the LDOS content  $N(\mathbf{r}, \omega, \mathbf{e}_d)\Delta\omega$  in each frequency bin, one needs to choose an appropriate  $\mathbf{k}$ -vector spacing  $\Delta k$  that depends on the steepness of the sampled dispersion relation  $\omega(\mathbf{k})$ .

Indeed, the useful frequency resolution  $\Delta\omega$  of a histogram of the DOS and LDOS is limited by the resolution  $\Delta k$  of the grid in  $\mathbf{k}$  space to

$$\Delta\omega \approx \Delta k |\nabla_{\mathbf{k}}\omega|, \quad (11)$$

as detailed in [45] for the electronic DOS. This criterion relates the separation between adjacent  $\mathbf{k}$ -grid points to their approximate frequency spacing via the group velocity. If histogram bins are chosen too narrow compared to the expected frequency spacing between contributions to the discretized LDOS integral, unphysical spikes appear in the approximation, especially in the limit of small  $\omega$ , where the group velocity  $|\nabla_{\mathbf{k}}\omega|$  is usually largest. Apart from full gaps in the LDOS, photonic crystals also promise sharp lines at which the LDOS is enhanced, which are important for nonclassical emission dynamics. Hence it is especially important to distinguish sharp spikes that are due to histogram binning noise from true features. Unfortunately, many reports in literature feature sharp spikes that are evidently binning noise (wave vector undersampling errors), as they occur in the long wavelength limit, below any stopgap.

To improve the resolution without adding time-consuming diagonalizations, several interpolation schemes have been suggested [45] to improve on discrete summation over the Monkhorst and Pack special sampling points. Interpolation schemes such as the improved linear tetrahedron method essentially assume that bands  $\omega_{n,\mathbf{k}}$  and mode contributions  $|\mathbf{e}_d \cdot \mathbf{E}_{n,\mathbf{k}}(\mathbf{r})|^2$  vary linearly be-

tween k-points [31]. Based on this assumption, interpolation schemes appear to require fewer k-points for accurate, smooth LDOS approximations without binning noise. However, they are still subject to a similar intrinsic relation [46] between required accuracy and chosen wave vector sampling density in Eq. (11) due to interpolation errors introduced by the curvature of  $\omega_{n,\mathbf{k}}$  at band edges, and the curvature that is expected in  $|\mathbf{e}_d \cdot \mathbf{E}_{n,\mathbf{k}}(\mathbf{r})|^2$ . On the basis of the underlying similarities between interpolation methods and special point weighted summations outlined in [46], we anticipate little computational benefit in implementing the linear tetrahedron method. This analysis is confirmed by the excellent agreement of our DOS results with results of Busch and John [31] that use the tetrahedron method with identical k-point density.

A good benchmark for the error in the  $\mathbf{k}$ -space integration, independent of the convergence of the plane-wave method, is to calculate the LDOS or DOS of an “empty” crystal, with uniform dielectric function equal to unity. Such an empty crystal represents a limit of zero photonic strength and the maximum possible group velocity  $|\nabla_{\mathbf{k}}\omega|$ . In Fig. 1 we show the DOS in an empty *fcc* crystal. As expected for a crystal with zero dielectric contrast, the calculated DOS is independent of dipole position and orientation. In agreement with the well-known DOS in vacuum the calculated DOS increases parabolically with frequency. Fluctuations around the parabola are due to binning noise associated with the finite  $\mathbf{k}$ -space discretization. We have calculated the relative root-mean-square error in the calculated density of states (DOS) for an *fcc* empty crystal averaged over all histogram bins in the frequency range  $0 < \omega a/2\pi c < 1$  for several combinations of histogram binwidth and  $\mathbf{k}$ -grid resolution, as specified in the caption of Fig. 2. As predicted by Eq. (11), the deviation of the approximation from the analytic result is inversely proportional to the ratio  $\Delta\omega/\Delta k$ .

In most cases, one wants to calculate the LDOS with a given frequency resolution  $\Delta\omega$ , i.e.,  $N(\mathbf{r}, \omega, \mathbf{e}_d)\Delta\omega$ , to within a predetermined accuracy. For instance, calculating the vacuum DOS for frequencies  $0 < \omega a/2\pi c < 1$  with a desired absolute accuracy better than  $0.01(4/a^2c)$  (1% of the vacuum DOS at  $\omega a/2\pi c = 1$ ) and a desired frequency resolution of  $\Delta\omega = 0.01(2\pi c/a)$  requires using  $\Delta k \sim \Delta\omega/0.3c$ . The number of k-points corresponding to this wave-vector sampling equals 2480 k-points in the irreducible wedge of the *fcc* Brillouin zone, 59 520 in the required

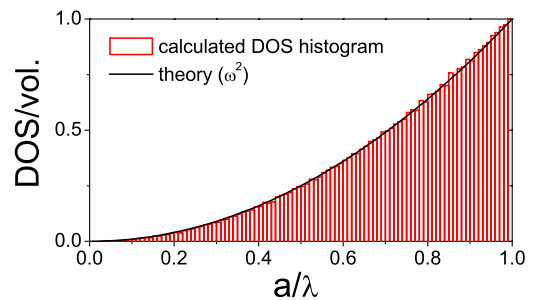


Fig. 1. (Color online) DOS per volume in units  $4/a^2c$  for vacuum modeled as an “empty” *fcc* crystal. The calculated DOS shown by histogram bars is compared to the analytically derived  $\omega^2$  behavior (curve). In vacuum the DOS per volume equals the dipole-averaged LDOS.

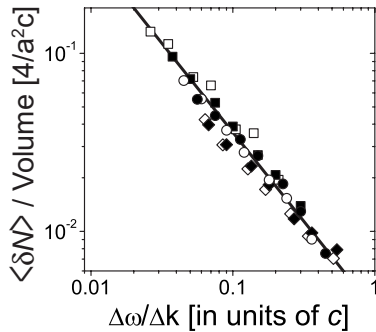


Fig. 2. Average absolute deviation of the calculated DOS from the exact total DOS  $N(\omega)$  for an “empty crystal.” The average runs over the frequency range  $0 < \omega < 2\pi c/a$ , and the deviation is in units of the DOS  $N(\omega)$  per volume at  $\omega a/2\pi c = 1$ , i.e., in units  $4/a^2c$ . In accordance with Eq. (11), the error is inversely proportional to the ratio  $\Delta\omega/\Delta k$  of the histogram bin width  $\Delta\omega$  to the integration grid spacing  $\Delta k$ . Symbols correspond to integration using  $N_k = 280, 770, 1300, 2480, 2992$ , and  $3570$  ( $\square, \blacksquare, \circ, \bullet, \diamond, \blacklozenge$ )  $k$ -points in the irreducible wedge of the Brillouin zone, with various  $\Delta\omega$ .

half Brillouin zone, or equivalently  $N_k = 119\,040$  in the full Brillouin zone.

Photonic crystals with nonzero index contrast cause a pronounced frequency structure of the LDOS. Due to the flattening of bands compared to the dispersion bands of empty crystals, the  $k$ -space integration itself is at least as accurate, assuming that the eigenfrequencies and the field-mode patterns are known with infinite accuracy. In practice, one needs to adjust the number of plane waves to obtain all eigenfrequencies to within the desired frequency resolution  $\Delta\omega$ . In our computations for *fcc* crystals, we represented the  $k$ -space of half of the first Brillouin zone by an equidistant grid consisting of  $N_k/2 = 145\,708$   $k$ -points. The frequency resolution of our LDOS histograms is  $\Delta\omega = 0.01$  ( $2\pi c/a$ ) and the spatial resolution of the LDOS is approximately  $a/40$  judging from the maximum  $|\mathbf{G} - \mathbf{G}'| \approx 120/a$  involved in the expansion with  $N_G = 725$  plane waves in Eq. (4).

#### D. Computation Time Required for LDOS

Calculating the LDOS in 3D periodic structures is a time-consuming task. The chosen degree of  $k$ -space discretization ( $N_k/2 = 145\,708$   $k$ -points) and the number of plane waves ( $N_G = 725$ ) are the result of a tradeoff between the desired accuracy and tolerated duration of the calculations. Essentially the computation consists of solving for the lowest  $n$  eigenvalues and eigenvectors of a real symmetric  $2N_G \times 2N_G$  matrix for each of the  $N_k$   $k$ -points independently. To accomplish this calculation, we use the standard Matlab “eigs” implementation [47] of an implicitly restarted Arnoldi method (ARPACK) that takes approximately 2.2 seconds to find the lowest 20 eigenvalues and eigenvectors of a single Hermitian  $1500 \times 1500$  (i.e.,  $N_G \approx 750$  plane waves) matrix on a 3 GHz Intel Pentium 4 processor, or on a 2.4 GHz Intel Core Duo processor. For 145 708  $k$ -points the resulting computation time is hence on the order of 90 h (4 days).

Since the Matlab ARPACK routine is already highly optimized, we do not expect that the computation time per  $k$ -point can be significantly reduced for LDOS calculations based on the standard H-field inverted-matrix

plane-wave method. In terms of the number of plane waves  $N_G$ , the computation time scales as  $N_G^3$ . As in [48], the algorithm can be accelerated by realizing that the iterative eigensolver does not require the full matrix  $\mathcal{H}$  multiplying the vector  $\mathbf{u}$  in Eq. (7), but rather a function that quickly computes the image  $\mathcal{H}\mathbf{u}$  of any trial vector  $\mathbf{u}$ . Since calculating  $\mathcal{H}\mathbf{u}$  repeatedly involves a slow matrix-vector multiplication with  $\eta_{\mathbf{G}-\mathbf{G}'}$ , the algorithm is accelerated only for  $N_G > 1000$ .

### 3. COMPARISON WITH PREVIOUS RESULTS

To test the computations, we compare our results with earlier reports. We have calculated the DOS and LDOS in an *fcc* crystal consisting of dielectric spheres with  $\epsilon_1 = 7.35$  ( $\text{TiO}_2$ ) in a medium with  $\epsilon_2 = 1.77$  (water)—the same structure as was analyzed in [31,33]. The spheres occupy 25 vol% of the crystal. Figure 3 shows the total DOS in this photonic crystal calculated by us and by Busch and John [31]. We reproduce the earlier calculations of the total DOS: both results shown in Fig. 3 are in excellent agreement, with deviations less than 2% throughout the frequency range  $0 < \omega a/2\pi c < 1$ .

In Fig. 4 (Media 1) we demonstrate the LDOS in the same photonic crystal at a specific location: a point equidistant from two nearest-neighbor spheres. In this calculation, we used the same number of reciprocal-lattice vectors  $N_G = 965$  as in the only available benchmark paper, by Wang *et al.* [33], that does not contain symmetry errors. We find that our calculations (histogram bars) are in good agreement up to  $a/\lambda = 0.85$  with the LDOS reported previously (solid curve): the deviations are less than 1%. Deviations at higher frequencies are due either to a difference in accuracy of  $k$ -space integration (frequency binning resolution and  $k$ -space sampling density) or to a difference in accuracy of the plane-wave methods (eigenmodes and eigenfrequencies). Unfortunately, neither the accuracy nor the frequency resolution is specified in [33]. The  $k$ -space sampling density in our work is approximately twice the density specified in [33]. Based on the excellent agreement of our total DOS calculations with those of Busch and John [31], and on the fact that Wang *et al.* used a  $k$ -space density and plane-wave number comparable with that of Busch and John, it is unlikely that

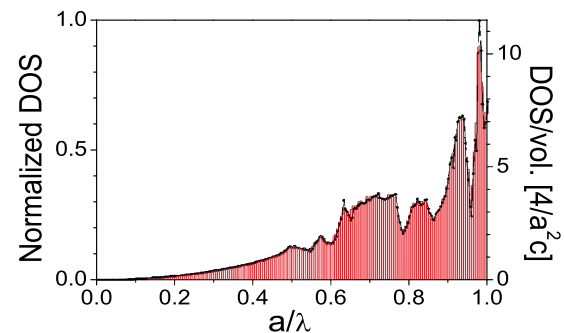


Fig. 3. (Color online) DOS per volume in an *fcc* crystal consisting of spheres with  $\epsilon = 7.35$  in a medium with  $\epsilon = 1.77$  and with a filling fraction of the spheres of 25 vol%. The solid dotted curve represents calculations from [31]. Our result is plotted as a histogram.

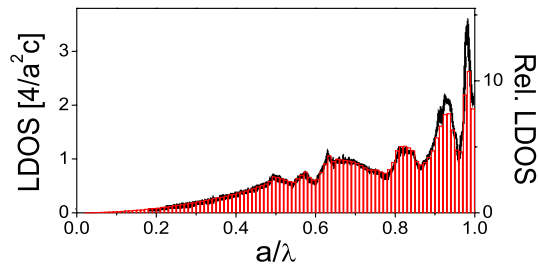


Fig. 4. (Color online) Dipole-averaged LDOS in the same photonic crystal as in Fig. 3 at a position  $\mathbf{r}=(1/4, 1/4, 0)$ . Histogram: our calculations (Media 1). Solid curve: results from [33]. This relative LDOS is the ratio of the LDOS to that in vacuum at  $a/\lambda=0.495$ .

inaccuracy of the  $k$ -space integration in either calculation is the source of discrepancy. We therefore surmise that deviations are due to a difference in the method of evaluation of  $\mathbf{E}_{n,\mathbf{k}}(\mathbf{r})$ . Conversion of  $\mathbf{D}$  to  $\mathbf{E}$  by multiplication with  $1/\epsilon(\mathbf{r})$  in real space as proposed in [33] can cause incorrect mode amplitudes due to Gibbs oscillations, as opposed to the Fourier space conversion using Eq. (8). In general our calculations confirm the result by Wang *et al.* [33] that the LDOS is correctly calculated only by integration over half the Brillouin zone, rather than over the irreducible part as was incorrectly used in earlier reports. Errors incurred by neglecting the lowered symmetry are large, as contributions from the 48 different irreducible wedges in the Brillouin zone differ up to tenfold.

#### 4. LDOS IN TiO<sub>2</sub> INVERSE OPALS

In recent time-resolved experiments, enhanced and inhibited emission rates were demonstrated for quantum dots embedded inside TiO<sub>2</sub> inverse opals [19,21,35]. Due to the large refractive index of TiO<sub>2</sub>, these crystals are strongly photonic as gauged by the fact that modes are forbidden for over  $2\pi$  sr in  $k$ -space for frequencies near first-order Bragg diffraction [49]. In the framework of these experiments, it is highly relevant to calculate the LDOS inside such inverse-opal photonic crystals, especially for the source positions occupied in experiments.

We model the position dependence of the dielectric function  $\epsilon(\mathbf{r})$  as shown in Fig. 5. This model assumes an infinite  $fcc$  lattice of air spheres with radius  $r=0.25\sqrt{2}a$  ( $a$  is the cubic lattice parameter). The spheres are covered by overlapping dielectric shells ( $\epsilon=6.5$ ) with outer radius  $1.09r$ . Neighboring air spheres are connected by cylindrical windows of radius  $0.4r$ . The resulting volume fraction of TiO<sub>2</sub> is equal to about  $\varphi=11.5\%$ . The structural parameters are inferred from detailed characterization of the inverse opals using electron microscopy and small-angle X-ray scattering [14,15]. Moreover, the stopgaps in the photonic band structure [Fig. 6 (Media 2 and Media 3)] calculated using this model agree well with reflectivity measurements in the ranges of both the first-order ( $a/\lambda=0.7$ ) and second-order Bragg diffraction ( $a/\lambda=1.2$ ) [50].

Henceforth, we will consider the relative LDOS, which is the ratio of the LDOS in a photonic crystal to that in a homogeneous medium with the same volume-averaged dielectric function ( $n_{av}=\sqrt{\epsilon_{av}}=1.277$  for the TiO<sub>2</sub> crystals). This scaling is motivated by experimental practice, in

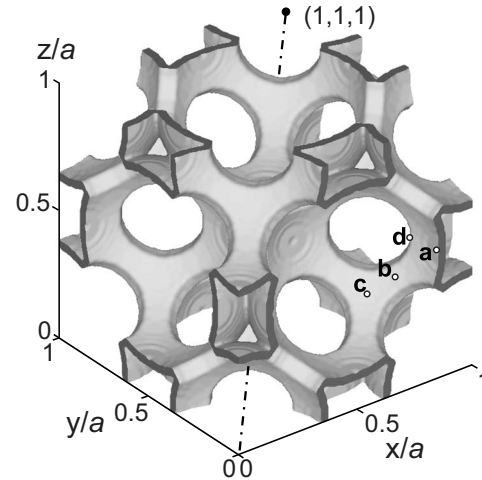


Fig. 5. Rendering of the dielectric function in one  $fcc$  unit cell that models the TiO<sub>2</sub> inverse-opal structure in Section 4: an  $fcc$  lattice of air spheres of radius  $r=0.25\sqrt{2}a$  with  $a$  being the cubic lattice parameter. The spheres are covered by shells with  $\epsilon=6.5$  and outer radius  $1.09r$ . Neighboring air spheres are connected by windows of radius  $0.4r$ . The letters  $\mathbf{a}$ – $\mathbf{d}$  indicate four different positions at the TiO<sub>2</sub>–air interface:  $\mathbf{a}=(1,0,0)/(2\sqrt{2})$ ,  $\mathbf{b}=(1,1,2)/(4\sqrt{3})$ ,  $\mathbf{c}=(1,1,1)/(2\sqrt{6})$ ,  $\mathbf{d}=(0.33,0.13,0)$  (points shown are symmetry-equivalents). The dashed-dotted line shows the body diagonal of the cubic unit cell.

which emission rate modifications are judged by normalizing measured rates to the emission rate of the same emitter in crystals with a much smaller lattice constant  $a$  [19,21,35]. In these reference systems, emission frequencies correspond to the effective medium limit  $a/\lambda \ll 0.5$  quantified by an average index. In units of  $4/a^2c$ , the LDOS in a homogeneous medium is equal to  $n_{av}(a/\lambda)^2/3$ , which is used as normalization for Figs. 7, 8, and 9.

As an alternative to the geometrically defined average index motivated by experimental practice, one can also extract an effective refractive index from the long-wavelength dispersion relation of the first bands, which yields a value  $\bar{n}_{eff}=1.216$ . Using this effective refractive index would scale the curves in Figs. 7–9 by a factor 1.05.

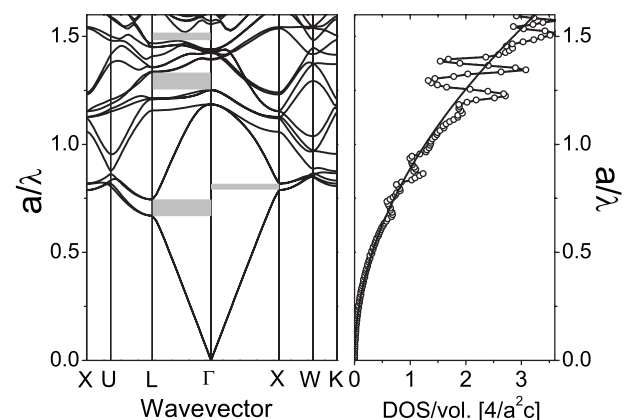


Fig. 6. Left side: Photonic band structure (Media 2) for the TiO<sub>2</sub> inverse opal shown in Fig. 5. The gray rectangles indicate stopgaps in the  $\Gamma L$  direction and one stopgap in the  $\Gamma X$  direction for the inverse opal. Right side: The stopgaps result in the decreased DOS as shown by open circles (Media 3) at corresponding frequencies compared to the DOS in a homogeneous medium with  $n_{av}=1.27$  as shown by the solid curve.

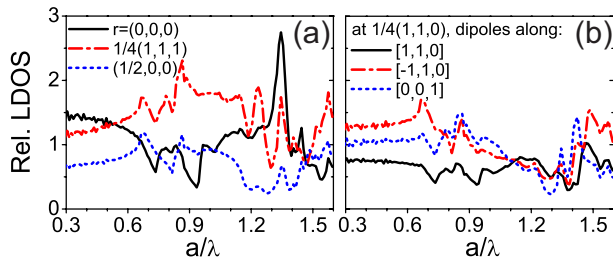


Fig. 7. (Color online) Relative LDOS in the inverse opal shown in Fig. 5 at three different positions: (a) (Media 4)  $\mathbf{r}=(0,0,0)$  [the center of an air sphere, solid curve],  $\mathbf{r}=1/4(1,1,1)$  [among three air spheres, dashed-dotted curve],  $\mathbf{r}=(1/2,0,0)$  [midway between two spheres along  $[1,0,0]$  direction, dotted curve]. (b) (Media 5) Relative LDOS at  $\mathbf{r}=1/4(1,1,0)$  [in the window between two spheres] projected on  $\mathbf{e}_d=[1,1,0]$ ,  $[-1,1,0]$ ,  $[0,0,1]$  directions shown by solid, dashed-dotted, dotted curves, respectively.

In Fig. 7(a) (Media 4) we plot the resulting LDOS at three positions in the unit cell: at  $\mathbf{r}=(0,0,0)$ ,  $1/4(1,1,1)$ , and  $(1/2,0,0)$ . As in the remainder of this paper, these real-space coordinates are expressed in units of the lattice spacing  $a$  relative to Cartesian basis vectors along the cubic unit cell axes (Fig. 5). Dipole directions  $\mathbf{e}_d$  will be quoted in square brackets  $[,\dots]$  relative to the same Cartesian basis, and are always assumed to be of unit length (even if not explicitly normalized). Because of the high symmetry of the points chosen for Fig. 7, the LDOS does not depend on the dipole orientation, as we verified explicitly.

A first main observation from Fig. 7(a) (Media 4) is that the LDOS differs considerably between these three positions at all reduced frequencies. This observation illustrates the well-known strong dependence of the LDOS on position within the unit cell of photonic crystals [10,27,31].

A second main observation in Fig. 7(a) (Media 4) is that the LDOS strongly varies with reduced frequency, revealing troughs and peaks caused by the pseudogap near  $a/\lambda=0.7$ , which is related to first-order stopgaps such as the L-gap. The effects of second-order stopgaps appear beyond  $a/\lambda > 1.15$  [50]. In the middle of the air region at position  $\mathbf{r}=(0,0,0)$  there is a sharp, factor-of-three enhancement at  $a/\lambda \approx 1.35$  within a narrow frequency range. This feature could be probed by resonant atoms infiltrated in the crystals [51]. At position  $\mathbf{r}=(1/2,0,0)$  in an interstitial, the mode density has a broad trough near  $a/\lambda=1.25$  that will lead to strongly inhibited emission.

A third main observation is that at spatial positions with low symmetry, the LDOS clearly depends on the orientation of the transition dipole moment. Figure 7(b) (Media 5) shows the frequency-dependent LDOS for three perpendicular dipole orientations at a position in the center of a window that connects two neighboring air spheres (see Fig. 5). The LDOS differs for all three orientations, and is thus anisotropic. At low frequency ( $a/\lambda=0.3$ ), the emission rate is highest for a dipole pointing in the  $\mathbf{e}_d=[-1,1,0]$  direction; with increasing frequency the highest rate shifts to  $\mathbf{e}_d=[0,0,1]$  and then to the  $\mathbf{e}_d=[1,1,0]$  orientation.

We emphasize that for emitters with fixed or slowly varying dipole orientations, such as dye molecules or

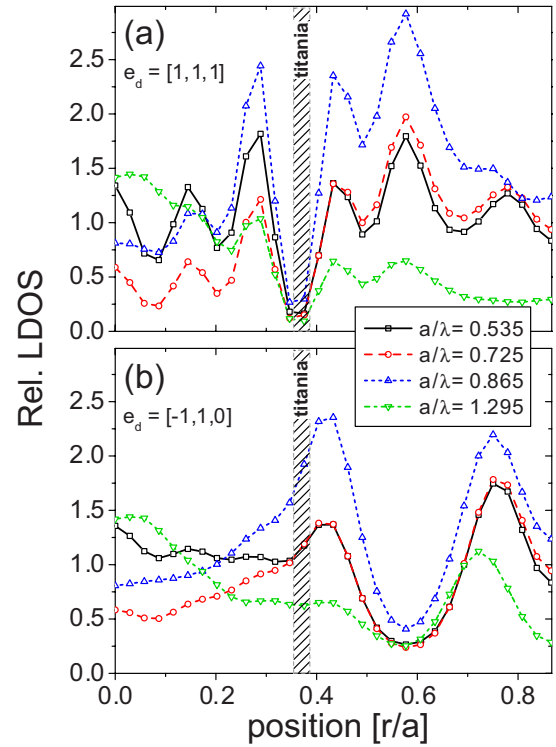


Fig. 8. (Color online) Relative LDOS at four key frequencies  $a/\lambda=0.535, 0.725, 0.865, 1.295$  in the inverse opal as a function of position  $r$  on the line from  $\mathbf{r}=(0,0,0)$  to  $\mathbf{r}=1/2(1,1,1)$ . The hatched boxes indicate the position of the dielectric  $\text{TiO}_2$  shell. The LDOS is projected on two dipole orientations: (a)  $\mathbf{e}_d=[1,1,1]$  perpendicular to the dielectric-air interface, (b)  $\mathbf{e}_d=[-1,1,0]$  parallel to the interface. The LDOS projected on the  $\mathbf{e}_d=[-1,-1,2]$  and  $\mathbf{e}_d=[-1,1,0]$  directions are equal. For  $r/a$  between  $\sqrt{3}/2$  and  $\sqrt{3}$  the LDOS is mirror-symmetric to that in the region from 0 to  $\sqrt{3}/2$ .

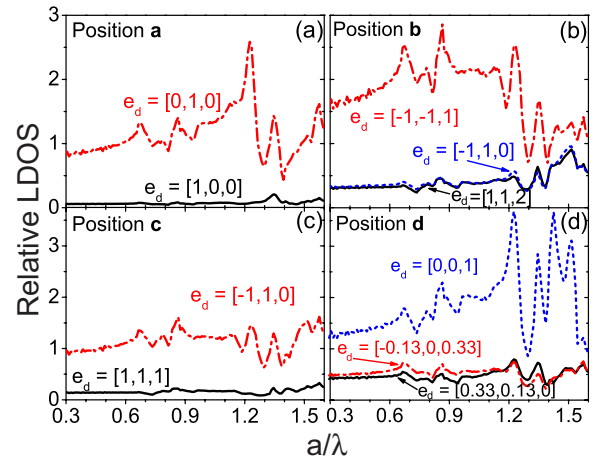


Fig. 9. (Color online) Relative LDOS in the inverse opal at four different positions on the  $\text{TiO}_2$ -air interface shown in Fig. 5. At each position the LDOS is projected on three mutually orthogonal dipole orientations  $\mathbf{e}_d$ . (a) (Media 6) Point **a** for  $\mathbf{e}_d=[1,0,0]$  and  $[0,1,0]$ ; the LDOS for  $\mathbf{e}_d=[0,0,1]$  is identical to that at  $\mathbf{e}_d=[0,1,0]$ . (b) (Media 7) Relative LDOS at point **b** for  $\mathbf{e}_d=[1,1,2]$ ,  $[-1,1,0]$ ,  $[-1,-1,1]$ . (c) (Media 8) Point **c** for  $\mathbf{e}_d=[1,1,1]$  and  $[-1,1,0]$ ; LDOS at  $\mathbf{e}_d=[-1,-1,2]$  is equal to that at  $\mathbf{e}_d=[-1,1,0]$ . (d) (Media 9) Relative LDOS at point **d** for  $\mathbf{e}_d=[0.33,0.13,0]$ ,  $[-0.13,0,0.33]$ ,  $[0,0,1]$ .

quantum dots on solid interfaces, the emission rate is determined by the optical modes that are projected on the dipole orientation. Therefore, knowledge of the projected LDOS is important for controlling spontaneous emission rates as well as for interpreting the data from experiments on emitters in photonic metamaterials.

A fourth main observation from Figs. 7(a) and 7(b) (Media 4 and 5) is that at low frequencies of  $a/\lambda < 0.5$ , the relative LDOS hardly varies with frequency, which means that the mode density is proportional to  $\omega^2$ , as in homogeneous media. Interestingly, there is a clear dependence of the LDOS on both the position and the dipole orientation even at these low frequencies, i.e., long wavelengths relative to the crystal periodicity. The reason for these effects is that the photonic Bloch modes exhibit local variations of the electric field related to local variations of the dielectric function in order to satisfy the continuity equations at dielectric boundaries for the parallel  $\mathbf{E}$  or perpendicular  $\mathbf{D}$  field, respectively [34,52]. Consequently, the LDOS strongly varies on length scales much less than the wavelength, i.e., even in the electrostatic or effective medium limit. While such behavior may appear surprising, its origin in electrostatic depolarization effects has been discussed before [52,53].

To gain more insight into the spatial dependence of the LDOS in the inverse opals, we have performed calculations for dipoles positioned along a characteristic axis in the unit cell. Figure 8 shows the LDOS at four key frequencies for dipoles placed on the body diagonal of the cubic unit cell, that is, on the line from  $\mathbf{r}=(0,0,0)$  to  $\mathbf{r}=1/2(1,1,1)$  in the  $[1,1,1]$  direction. The LDOS has clear maxima and minima along the diagonal, varying by more than ten times. Figure 8(a) shows that for a dipole oriented in the  $\mathbf{e}_d=[1,1,1]$  direction (perpendicular to the dielectric–air interface), the LDOS is strongly ( $>5\times$ ) suppressed near the dielectric  $\text{TiO}_2$  shell ( $r/a \approx 0.353$ ) at all frequencies. In contrast, no strong suppression or enhancement occurs for dipole orientations parallel to the dielectric interface; see Fig. 8(b).

The strongly differing LDOS for dipoles near the dielectric rationalize the broad distributions of emission rates that were recently observed for quantum dots in inverse opals [35]; see below. Enhancements and inhibitions also occur in the air regions: the LDOS is enhanced at  $r/a \approx 0.28$  and  $0.57$  by up to 2.5 to 3 times, respectively; see Fig. 8(a). At point  $r/a=1/\sqrt{3} \approx 0.57$  that lies in the air region in the lattice plane defined by Miller indices (111), the LDOS is inhibited at all frequencies for the dipole orientations  $\mathbf{e}_d=[-1,1,0]$  and  $[-1,-1,2]$  that are perpendicular to the (111) plane [see Fig. 8(b)]. Finally, for dipoles parallel to the body diagonal [Fig. 8(a)] the mode density shows pseudo-oscillatory behavior on length scales much less than the wavelength, e.g., a period of  $0.2a$  at frequency  $0.535a/\lambda$  (period corresponds to  $1/10$  of a wavelength). This observation confirms that photonic crystals are *bona fide* metamaterials where optical properties strongly vary on length scales much less than the wavelength.

In recent time-resolved experiments [21,35], emission from quantum dot light sources distributed at the internal  $\text{TiO}_2$ –air interfaces of the inverse opals was investigated. To analyze the experimental data, we have calcu-

lated the LDOS at several symmetry-inequivalent positions on the  $\text{TiO}_2$  shells: at points  $\mathbf{a}$ ,  $\mathbf{b}$ ,  $\mathbf{c}$ , and  $\mathbf{d}$  (see Fig. 5) for three mutually orthogonal orientations of the emitting dipole, where the first orientation is chosen along the vector pointing from  $\mathbf{r}=(0,0,0)$  toward the corresponding point. Figures 9(a)–9(d) (Media 6 7 8 9) show that at all these positions the LDOS strongly varies with reduced frequency and position, as expected, and also with orientation of the dipole. In broad terms, for a dipole parallel to the interface the LDOS is near 1 at low frequency and increases to a peak enhancement of 2.5 times at  $a/\lambda=1.22$  before strongly varying at high frequencies. For reference, the frequency  $a/\lambda=1.22$  is in the range where a bandgap is expected for more strongly interacting crystals. The plots also reveal that for dipoles perpendicular to the  $\text{TiO}_2$ –air interface, the LDOS is strongly inhibited (more than ten times) over broad frequency ranges. For instance, Fig. 9(a) shows that the emission rate for a dipole perpendicular to the interface is 16-fold inhibited to a level of 0.06, with a maximum of 0.22 (fivefold inhibition) at  $a/\lambda=1.22$ . It is striking that the strong inhibition occurs over a broad frequency range from 0.3 to 1.6, i.e., more than two octaves in frequency. While the inhibition is not complete, the bandwidth is much larger than the maximum bandwidth of 12% for a full 3D bandgap in inverse opals [54] and far exceeds the bandwidth of the 2D gap for TE modes in membrane photonic crystals, which allows a sevenfold inhibition [26,30] over a 30% bandwidth.

In the frequency range up to  $a/\lambda=1.1$ , the dependence of the LDOS on frequency is quite similar at all the positions and dipole orientations. This remarkable result agrees with the experimental observation from [35]: the complex decay curves of light sources in the inverse opals are described by one and the same functional shape (log-normal) of the decay rate distribution for all reduced frequencies studied. For the interpretation of the time-resolved experiments on ensembles of emitters in the inverse-opal photonic crystals, the results presented above mean that

1. the decay rate of an individual emitter is determined by its frequency and position, and also by the orientation of its transition dipole in the photonic crystal;
2. the measured spontaneous-emission decay depends on how the emitters are distributed in the crystal;
3. even in the low-frequency regime, ensemble measurements will reveal nonexponential decay curves;
4. the similar shape of the reduced-frequency dependence of the LDOS allows modeling of the nonexponential decay curves with a single type of decay-rate distribution; in other words, one distribution function can be successfully used to model the multiexponential decay curves measured from crystals with different lattice parameters.

## 5. LDOS IN SILICON INVERSE OPALS

A complete inhibition of spontaneous emission may be achieved only in photonic crystals with a 3D photonic bandgap. Therefore, there has been much effort to fabricate inverse opals from silicon rather than titania, since the higher index of silicon allows for a photonic bandgap

[31,39]. For the calculation of the LDOS in such Si inverse opals, the dielectric function  $\epsilon(\mathbf{r})$  was modeled similarly to that in the inverse opals shown in Fig. 5. From SEM observations we inferred the following structural parameters [17,18]: the outer radius of the overlapping dielectric shells with  $\epsilon=11.9$  is about  $1.15r$  (where  $r=0.25\sqrt{2}a$  is the air-sphere radius, and  $a$  is the lattice parameter). The cylindrical windows connecting neighboring air spheres have a radius of  $0.2r$ . The larger outer radius and the smaller window size compared with the  $\text{TiO}_2$  inverse opals are commensurate with a higher volume fraction of about 22% Si [18].

The band structure and total DOS for this system are shown in Fig. 10 (Media 10 and Media 11). The DOS is strongly depleted in a pseudogap between the second and third bands [38] at frequencies near  $a/\lambda=0.55$ . Near frequency  $a/\lambda=0.85$ , both the band structures and the DOS reveal a 3D photonic bandgap of relative width  $\Delta\omega/\omega \approx 3\%$  between the eighth and ninth bands [31]. Compared with the  $\text{TiO}_2$  structure, both the lowest-order L-gap and the eighth and ninth bands are shifted to lower reduced frequencies. This shift is the result of the higher effective refractive index of the Si inverse opals, on account of a higher index of the backbone and a higher filling fraction.

Figure 11(a) (Media 12) presents the relative LDOS at three high-symmetry positions in the unit cell  $\mathbf{r}=(0,0,0)$ ,  $1/4(1,1,1)$  and  $(1/2,0,0)$ . The LDOS is normalized to the LDOS for a homogeneous medium with  $n_{\text{av}}=\sqrt{\epsilon_{\text{av}}}=1.88$ . Alternatively, the long-wavelength dispersion of the crystal sets  $\tilde{n}_{\text{eff}}=1.65$ , which when used as normalization would scale the curves in Fig. 11 by a factor of 1.14. The LDOS varies much more strongly with frequency than in  $\text{TiO}_2$  inverse opals as a result of the larger dielectric contrast that leads to strongly modified dispersion relations and Bloch mode profiles. While the maxima up to 3.2 are not much higher than in  $\text{TiO}_2$  inverse opals, the minima in the mode density are reduced and the slopes are steeper. As expected, the LDOS is completely inhibited at all positions in the frequency range of the bandgap. Previously, it has been suggested that the LDOS could be inhibited at salient positions in the unit cell for frequencies outside a complete gap. While Fig. 11(a) (Media 12) reveals that the mode density is strongly reduced above the

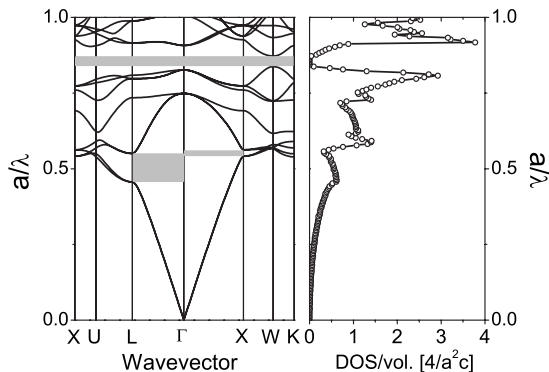


Fig. 10. Left side: Photonic band structure (Media 10) for an inverse opal from silicon ( $\epsilon=11.9$ ). Right side: The total DOS in the Si inverse opal (Media 11). The DOS is strongly depleted for frequencies near  $\Gamma\text{L}$  and  $\Gamma\text{X}$  stopgaps (gray rectangles). A photonic bandgap (gray bar) occurs between bands 8 and 9, as also reflected in the vanishing DOS.

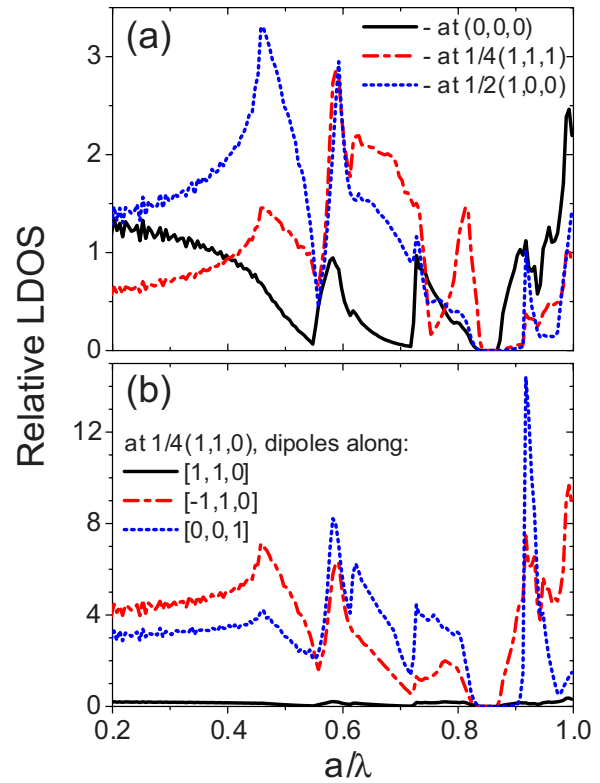


Fig. 11. (Color online) Relative LDOS in a Si inverse opal at (a) (Media 12)  $\mathbf{r}=(0,0,0)$  [the center of an air sphere, solid curve],  $\mathbf{r}=1/4(1,1,1)$  [among three air spheres, dashed-dotted curve],  $\mathbf{r}=(1/2,0,0)$  [midway between two spheres along  $[1,0,0]$  direction, dotted curve]; (b) (Media 13) Relative LDOS at  $\mathbf{r}=1/4(1,1,0)$  [in the window between two air spheres] projected on  $\mathbf{e}_d=[1,1,0]$ ,  $[-1,1,0]$ , and  $\mathbf{e}_d=[0,0,1]$  directions shown by solid, dashed-dotted, dotted curves, respectively.

bandgap, e.g., at  $\mathbf{r}=(1/2,0,0)$ , it is not truly inhibited. In fact, in the course of our study, we have not encountered any “sweet spots” where the LDOS is completely inhibited at frequencies outside a 3D photonic bandgap.

Figure 11(b) (Media 13) shows the LDOS at a lower symmetry position  $\mathbf{r}=1/4(1,1,0)$  in the window between two nearest-neighbor air spheres. The mode density has been calculated for three perpendicular dipole orientations. Figure 11(b) (Media 13) shows that the LDOS is highly anisotropic since it differs for all three orientations: at low frequencies ( $a/\lambda < 0.5$ ), the mode density is highest for the  $\mathbf{e}_d=[-1,1,0]$  orientation, intermediate for the  $[0,0,1]$  orientation, and lowest for the  $\mathbf{e}_d=[1,1,0]$  orientation. With increasing frequency, the highest LDOS also changes to other orientations, with the  $\mathbf{e}_d=[0,0,1]$  orientation having the highest LDOS above the pseudogap and even a narrow peak at frequency 0.95. Therefore, if it is possible to orient a quantum emitter with its dipole parallel to  $\mathbf{e}_d=[0,0,1]$ , this frequency range is conducive to strong emission enhancement and perhaps even quantum electrodynamic effects beyond weak coupling. Interestingly, these frequencies are slightly higher than the upper edge of the bandgap, where strong coupling effects have recently been discussed [12].

## 6. CONCLUSIONS

We have performed intensive calculations of the local density of states in  $\text{TiO}_2$  and Si inverse opals with experimen-

tally relevant structural parameters. Since conflicting and incorrect reports have previously appeared on the LDOS in photonic crystals, we set out to validate our method of choice, i.e., the H-field plane-wave expansion method. This validation relied on comparison with literature results, on the explicit verification of required symmetries that previous reports failed to satisfy, and on quantitative considerations of resolution and accuracy. Results for each structure are made available for other workers in the field, both as benchmarks and for comparison with experimental data. With the help of these computations we have obtained quantitative insight into the LDOS relevant for time-resolved ensemble fluorescence measurements on photonic crystals, such as have been obtained in recent experimental work [35]. The results of our numerical calculations reveal a surprisingly strong dependence of the LDOS on the orientation of the emitting dipoles.

## ACKNOWLEDGMENTS

We thank Dries van Oosten for careful reading of the manuscript. This work is part of the research program of the “Stichting voor Fundamenteel Onderzoek der Materie (FOM),” which is financially supported by the “Nederlandse Organisatie voor Wetenschappelijk Onderzoek (NWO).” AFK and WLW were supported by VENI and VICI fellowships funded by NWO. WLW also acknowledges funding by the Dutch Technology Foundation (STW) and NanoNed.

## REFERENCES

- J. D. Joannopoulos, S. G. Johnson, J. N. Winn, and R. D. Meade, *Photonic Crystals: Molding the Flow of Light*, 2nd ed. (Princeton U. Press, 2008).
- Photonic Crystals and Light Localization in the 21st Century*, C. M. Soukoulis, ed. (Kluwer, 2001).
- V. P. Bykov, “Spontaneous emission in a periodic structure,” *Sov. Phys. JETP* **35**, 269–273 (1972).
- V. P. Bykov, “Spontaneous emission from a medium with a band spectrum,” *Sov. J. Quantum Electron.* **4**, 861–871 (1975).
- E. Yablonovitch, “Inhibited spontaneous emission in solid-state physics and electronics,” *Phys. Rev. Lett.* **58**, 2059–2062 (1987).
- S. John, “Strong localization of photons in certain disordered dielectric superlattices,” *Phys. Rev. Lett.* **58**, 2486–2489 (1987).
- O. Painter, R. K. Lee, A. Scherer, A. Yariv, J. D. O’Brien, P. D. Dapkus, and I. Kim, “Two-dimensional photonic bandgap defect mode laser,” *Science* **284**, 1819–1821 (1999).
- H.-G. Park, S.-H. Kim, S.-H. Kwon, Y.-G. Ju, J.-K. Yang, J.-H. Baek, S.-B. Kim, and Y.-H. Lee, “Electrically driven single-cell photonic crystal laser,” *Science* **305**, 1444–1447 (2004).
- M. Grätzel, “Photoelectrochemical cells,” *Nature* **414**, 338–344 (2001).
- R. Sprik, B. A. van Tiggelen, and A. Lagendijk, “Optical emission in periodic dielectrics,” *Europhys. Lett.* **35**, 265–270 (1996).
- N. Vats, S. John, and K. Busch, “Theory of fluorescence in photonic crystals,” *Phys. Rev. A* **65**, 043808 (2002).
- P. Kristensen, A. F. Koenderink, P. Lodahl, B. Tromborg, and J. Mørk, “Fractional decay of quantum dots in real photonic crystals,” *Opt. Lett.* **33**, 1557–1559 (2008).
- Photonic Crystals. Advances in Design, Fabrication, and Characterization*, K. Busch, S. Lölkes, R. B. Wehrspohn, and H. Föll, ed. (Wiley-VCH Verlag GmbH, 2004).
- J. E. G. J. Wijnhoven and W. L. Vos, “Preparation of photonic crystals made of air spheres in titania,” *Science* **281**, 802–804 (1998).
- J. E. G. J. Wijnhoven, L. Bechger, and W. L. Vos, “Fabrication and characterization of large macroporous photonic crystals in titania,” *Chem. Mater.* **13**, 4486–4499 (2001).
- A. A. Zakhidov, R. H. Baughman, Z. Iqbal, C. Cui, I. Khayrullin, S. O. Dantas, J. Marti, and V. G. Ralchenko, “Carbon structures with three-dimensional periodicity at optical wavelengths,” *Science* **282**, 897–901 (1998).
- A. Blanco, E. Chomski, S. Grabtchak, M. Ibisate, S. John, S. W. Leonard, C. López, F. Meseguer, H. Míguez, J. P. Mondia, G. A. Ozin, O. Toader, and H. M. van Driel, “Large-scale synthesis of a silicon photonic crystal with a complete three-dimensional bandgap near 1.5 micrometres,” *Nature* **405**, 437–440 (2000).
- Y. A. Vlasov, X. Z. Bo, J. C. Sturm, and D. J. Norris, “On-chip natural assembly of silicon photonic bandgap crystals,” *Nature* **414**, 289–293 (2001).
- A. F. Koenderink, L. Bechger, H. P. Schriemer, A. Lagendijk, and W. L. Vos, “Broadband fivefold reduction of vacuum fluctuations probed by dyes in photonic crystals,” *Phys. Rev. Lett.* **88**, 143903 (2002).
- S. Ogawa, M. Imada, S. Yoshimoto, M. Okato, and S. Noda, “Control of light emission by 3D photonic crystals,” *Science* **305**, 227–229 (2004).
- P. Lodahl, A. F. van Driel, I. S. Nikolaev, A. Irman, K. Overgaag, D. Vanmaekelbergh, and W. L. Vos, “Controlling the dynamics of spontaneous emission from quantum dots by photonic crystals,” *Nature* **430**, 654–657 (2004).
- A. Badolato, K. Hennessy, M. Atatüre, J. Dreiser, E. Hu, P. M. Petroff, and A. Imamoglu, “Deterministic coupling of single quantum dots to single nanocavity modes,” *Science* **308**, 1158–1161 (2005).
- A. Kress, F. Hofbauer, N. Reinelt, M. Kaniber, H. J. Krenner, R. Meyer, G. Böhm, and J. J. Finley, “Manipulation of the spontaneous emission dynamics of quantum dots in two-dimensional photonic crystals,” *Phys. Rev. B* **71**, 241304 (2005).
- M. Fujita, S. Takahashi, Y. Tanaka, T. Asano, and S. Noda, “Simultaneous inhibition and redistribution of spontaneous light emission in photonic crystals,” *Science* **308**, 1296–1298 (2005).
- D. Englund, D. Fattal, E. Waks, G. Solomon, B. Zhang, T. Nakaoka, Y. Arakawa, Y. Yamamoto, and J. Vučković, “Controlling the spontaneous emission rate of single quantum dots in a two-dimensional photonic crystal,” *Phys. Rev. Lett.* **95**, 013904 (2005).
- B. Julsgaard, J. Johansen, S. Stobbe, T. Stolberg-Rohr, T. Sünner, M. Kamp, A. Forchel, and P. Lodahl, “Decay dynamics of quantum dots influenced by the local density of optical states in two-dimensional photonic crystal membranes,” *Appl. Phys. Lett.* **93**, 094102 (2008).
- T. Suzuki and P. K. L. Yu, “Emission power of an electric dipole in the photonic band structure of the fcc lattice,” *J. Opt. Soc. Am. B* **12**, 570–582 (1995).
- R. K. Lee, Y. Xu, and A. Yariv, “Modified spontaneous emission from a two-dimensional photonic bandgap crystal slab,” *J. Opt. Soc. Am. B* **17**, 1438–1442 (2000).
- C. Hermann and O. Hess, “Modified spontaneous emission rate in an inverted-opal structure with complete photonic bandgap,” *J. Opt. Soc. Am. B* **19**, 3013–3018 (2002).
- A. F. Koenderink, M. Kafesaki, C. M. Soukoulis, and V. Sandoghdar, “Spontaneous emission control in two-dimensional photonic crystal membranes,” *J. Opt. Soc. Am. B* **23**, 1196–1206 (2006).
- K. Busch and S. John, “Photonic band gap formation in certain self-organizing systems,” *Phys. Rev. E* **58**, 3896–3908 (1998).
- Z.-Y. Li, L.-L. Lin, and Z.-Q. Zhang, “Spontaneous emission from photonic crystals: full vectorial calculations,” *Phys. Rev. Lett.* **84**, 4341–4344 (2000).

33. R. Wang, X.-H. Wang, B.-Y. Gu, and G.-Z. Yang, "Local density of states in three-dimensional photonic crystals: calculation and enhancement effects," *Phys. Rev. B* **67**, 155114 (2003).
34. D. P. Fussell, R. C. McPhedran, and C. M. de Sterke, "Three-dimensional Green's tensor, local density of states, and spontaneous emission in finite two-dimensional photonic crystals composed of cylinders," *Phys. Rev. E* **70**, 066608 (2004).
35. I. S. Nikolaev, P. Lodahl, A. F. van Driel, A. F. Koenderink, and W. L. Vos, "Strongly nonexponential time-resolved fluorescence of quantum-dot ensembles in three-dimensional photonic crystals," *Phys. Rev. B* **75**, 115302 (2007).
36. A. F. Koenderink, A. Lagendijk, and W. L. Vos, "Optical extinction due to intrinsic structural variations of photonic crystals," *Phys. Rev. B* **72**, 153102 (2005).
37. A. A. Krokhnin and P. Halevi, "Influence of weak dissipation on the photonic band structure of periodic composites," *Phys. Rev. B* **53**, 1205–1214 (1996).
38. K. M. Ho, C. T. Chan, and C. M. Soukoulis, "Existence of a photonic gap in periodic dielectric structures," *Phys. Rev. Lett.* **65**, 3152–3155 (1990).
39. H. S. Sözüer, J. W. Haus, and R. Inguva, "Photonic bands: convergence problems with the plane-wave method," *Phys. Rev. B* **45**, 13962–13972 (1992).
40. J. D. Jackson, *Classical Electrodynamics* (Wiley, 1975).
41. V. Kuzmiak, A. A. Maradudin, and F. Pincemin, "Photonic band structures of two-dimensional systems containing metallic components," *Phys. Rev. B* **50**, 16835–16844 (1994).
42. N. W. Ashcroft and N. D. Mermin, *Solid State Physics* (Holt, Rinehart and Winston, 1976).
43. L. Li, "Use of Fourier series in the analysis of discontinuous periodic structures," *J. Opt. Soc. Am. A* **13**, 1870–1876 (1996).
44. H. J. Monkhorst and J. D. Pack, "Special points for Brillouin-zone integration," *Phys. Rev. B* **13**, 5188–5192 (1976).
45. G. Gilat, "Analysis of methods for calculating spectral properties in solids," *J. Comput. Phys.* **10**, 432–465 (1972).
46. P. E. Blöchl, O. Jepsen, and O. K. Andersen, "Improved tetrahedron method for Brillouin-zone integrations," *Phys. Rev. B* **49**, 16223–16233 (1994).
47. R. B. Lehoucq, D. C. Sorensen, and C. Yang, *ARPACK Users Guide: Solution of Large-Scale Eigenvalue Problems with Implicitly Restarted Arnoldi Methods* (SIAM Publications, 1998).
48. S. G. Johnson and J. D. Joannopoulos, "Block-iterative frequency-domain methods for Maxwell's equations in a planewave basis," *Opt. Express* **8**, 173–190 (2001).
49. M. S. Thijssen, R. Sprik, J. E. G. J. Wijnhoven, M. Megens, T. Narayanan, A. Lagendijk, and W. L. Vos, "Inhibited light propagation and broad band reflection in photonic air-sphere crystals," *Phys. Rev. Lett.* **83**, 2730–2733 (1999).
50. W. L. Vos and H. M. van Driel, "Higher order Bragg diffraction by strongly photonic fcc crystals: onset of a photonic bandgap," *Phys. Lett. A* **272**, 101–106 (2000).
51. P. J. Harding, "Photonic crystals modified by optically resonant systems," Ph.D. thesis (University of Twente, 2008), ISBN 978-90-365-2683-8, available from <http://www.photonicbandgaps.com>.
52. L. Rogobete, H. Schniepp, V. Sandoghdar, and C. Henkel, "Spontaneous emission in nanoscopic dielectric particles," *Opt. Lett.* **28**, 1736–1738 (2003).
53. H. Miyazaki and K. Ohtaka, "Near-field images of a monolayer of periodically arrayed dielectric spheres," *Phys. Rev. B* **58**, 6920–6937 (1998).
54. A. F. Koenderink, "Emission and transport of light in photonic crystals," Ph.D. thesis (University of Amsterdam, 2003). ISBN 90-9016903-2, available from <http://www.koenderink.info>.